Intermodal Brillouin scattering in solid-core photonic crystal fibers ⒻF

Paulo F. Jarschel, Erick Lamilla, Yovanny A. V. Espinel, et al.

COLLECTIONS

Ⓕ   This paper was selected as Featured

View Online   **Export Citation**   **CrossMark**

ARTICLES YOU MAY BE INTERESTED IN

Brillouin optomechanics in nanophotonic structures
APL Photonics **4**, 071101 (2019); https://doi.org/10.1063/1.5088169

Observing distant objects with a multimode fiber-based holographic endoscope
APL Photonics **6**, 036112 (2021); https://doi.org/10.1063/5.0038367

Versatile silicon microwave photonic spectral shaper
APL Photonics **6**, 036106 (2021); https://doi.org/10.1063/5.0033516

Intermodal Brillouin scattering in solid-core photonic crystal fibers Ⓕ

Paulo F. Jarschel,[1,2,a] ⓘD Erick Lamilla,[1,2] Yovanny A. V. Espinel,[1,2] Ivan Aldaya,[1,3] Julian L. Pita,[1,2,4] Andres Gil-Molina,[2,4] Gustavo S. Wiederhecker,[1,2] ⓘD and Paulo Dainese[1,2,5]

AFFILIATIONS

[1] Photonics Research Center, University of Campinas, Campinas 13083-859, SP, Brazil
[2] Gleb Wataghin Physics Institute, University of Campinas, Campinas 13083-859, SP, Brazil
[3] Campus of São João da Boa Vista, State University of São Paulo, São João da Boa Vista 13876-750, Brazil
[4] School of Electrical Engineering, University of Campinas, Campinas 13083-852, SP, Brazil
[5] Corning Research & Development Corporation, One Science Drive, Corning, New York 14830, USA

[a] Author to whom correspondence should be addressed: jarschel@ifi.unicamp.br

ABSTRACT

We investigate intermodal forward Brillouin scattering in a solid-core photonic crystal fiber (PCF), demonstrating efficient power conversion between the HE_{11} and HE_{21} modes, with a maximum gain coefficient of 21.4 W^{-1} km^{-1}. By exploring mechanical modes of different symmetries, we observe both polarization-dependent and polarization-independent intermodal Brillouin interaction. Finally, we discuss the role of squeeze film air damping and leakage mechanisms, ultimately critical to the engineering of PCF structures with enhanced interaction between high-order optical modes through flexural mechanical modes.

I. INTRODUCTION

Applications exploring optical waveguides and cavities supporting multiple spatial modes have greatly expanded in recent years. Albeit previously considered as an impairment for optical communications, multimode systems regained attention as the basis of mode division multiplexing (MDM)[1,2] and can substantially enhance the capabilities in many other applications such as sensing,[3–6] particle manipulation,[7–9] and nonlinear optical devices, for example, in frequency comb generation in multimode ring resonators[10] and non-reciprocal devices based on Brillouin scattering in multimode waveguides.[11,12] Excitation of different spatial modes can be performed using various approaches such as electronically addressable spatial light modulators (SLMs),[13–16] photonic lanterns,[17,18] and integrated mode combiners/multiplexers.[19] However, interaction between propagating modes is more difficult to achieve, despite being a crucial functionality for all-optical systems, as in switching, mode conversion, and optical isolators. Nonlinear optical effects offer a path to enable and control intermodal interactions, for example, using Kerr-induced long period gratings to perform all-optical mode conversion.[20] Stimulated Brillouin scattering (SBS) is another nonlinear mechanism that can be explored for intermodal interaction, with unique properties.[21–25] Besides enabling direct power exchange between different spatial modes, SBS can be explored as a mode-selective isolator or mode-selective variable optical attenuator (VOA)[26,27] and has recently been explored as the basis for non-reciprocal devices.[11,12]

Intermodal Brillouin scattering can occur between modes that are co-propagating or counter-propagating, respectively, referred to as forward Brillouin scattering (FBS) or backward Brillouin scattering (BBS).[21] In integrated silicon waveguides, high intermodal Brillouin gain has been recently reported.[28,29] In fibers, although the optomechanical coupling between two modes has been studied in dual-nanoweb fibers recently,[30] the first demonstration of stimulated intermodal FBS was obtained in all-solid fibers,[22,31] with relatively low gain. Efficient experimental demonstrations were only obtained in BBS configuration using few-mode fibers (FMFs).[23–25] As an alternative, solid-core PCFs offer enhanced optomechanical interactions due to the greater flexibility to engineer both optical and mechanical modal properties.[32–40] This versatility has been previously explored

for intramodal FBS,[36] and in this paper, we provide a comprehensive experimental and theoretical analysis of intermodal FBS in a PCF. By exploring multiple mechanical resonances, we show that both polarization-independent and polarization-dependent interaction can be implemented and demonstrate a *forward* intermodal Brillouin gain coefficient comparable to *backward* Brillouin-based mode conversion in FMFs. Finally, we investigate the fundamental limitations to conversion efficiency imposed by different forms of mechanical dissipation and discuss possible future enhancements.

II. PHASE-MATCHING AND SYMMETRY CONSIDERATIONS

In intermodal FBS, depicted in Fig. 1(a), optical forces generated by the beating of two optical modes selectively excite mechanical modes in the fiber, which, in turn, induce power exchange between the optical modes as they propagate. In particular, we investigate the interaction between the fundamental HE_{11} mode and one of the high-order HE_{21} modes, employed as pump and probe (Stokes line), respectively. Efficient interaction occurs when both energy and momentum are conserved, i.e., $\omega_p = \omega_s + \Omega$ and $\beta_p = \beta_s + q$, where Ω, ω_p, and ω_s are the mechanical, pump, and Stokes angular frequencies, respectively, and q, β_p, and β_s are the corresponding propagation constants [Fig. 1(b)]. In practice, these conditions yield a process that is highly frequency selective, as the pump–Stokes frequency detuning must match the frequency of a given mechanical mode within the mechanical resonance linewidth, typically in the order of megahertz. This property enables Brillouin-based devices to be highly wavelength selective. Another necessary condition is imposed by spatial symmetry selection rules. Following conventional mode coupling notation, the optomechanical coupling coefficient is proportional to the spatial overlap of the interacting fields,[21]

$$\langle \vec{E}_p \mid \delta\tilde{\varepsilon} \mid \vec{E}_s \rangle = \int_S \vec{E}_p^* \cdot \boldsymbol{\delta\varepsilon}^* \cdot \vec{E}_s \, dS \neq 0, \tag{1}$$

where S is the fiber cross section, $\vec{E}_p^*$ and $\vec{E}_s$ are the pump and Stokes electric field profiles, respectively, and $\boldsymbol{\delta\varepsilon}$ is the tensor of the permittivity perturbation induced by the mechanical mode. In our particular case, E_p and E_S exhibit even and odd reflection symmetry,

respectively. As a result, the mechanical modes must induce a perturbation with odd symmetry to yield a non-zero overlap integral. This is satisfied, for example, by a flexural mechanical mode, as illustrated in Fig. 1(c). In the particular case of PCFs, several mechanical modes satisfy both phase-matching and the spatial overlap selection rule, opening possibilities to explore novel mode-conversion functionalities in a wide range of discrete frequencies with or without polarization selectivity.

III. EXPERIMENTAL SETUP

The setup used in our experiments is illustrated in Fig. 2. On the launch side, both pump and Stokes lasers propagate in free-space. The Stokes beam reflects off a SLM, which can dynamically transform the phase profile of an incident beam, resulting in the excitation of one of the supported high-order modes (see Sec. S2.A of the supplementary material). A half-wave plate is used to adjust the Stokes polarization to match that of one of the HE_{21} modes, which are roughly linearly polarized. The pump polarization is adjusted to be either parallel or orthogonal to Stokes (referred to as x and y axes from here on). Both beams are then combined and launched into the fiber.

Low repetition rate pulses are used for both pump and Stokes (generated using external modulators) in order avoid power damages to the SLM. Such a pulsed scheme also helps identifying the optical modes excited through their group delay differences (see Sec. S2.A of the supplementary material for details). Initially, in order to optimize the SLM phase masks and characterize the excitation of various guided optical modes, we blocked off the pump beam and used short 35 ps pulses (at a repetition rate of 155 MHz) for the Stokes signal. The output of the PCF was split to enable simultaneous imaging of the beam via an InGaAs camera and detect the output pulses with a 20 GHz photodiode. Figure 2(b) shows the output pulses, alongside with the output beam profiles for a blank SLM phase mask (red) and a phase profile optimized to excite one of the HE_{21} modes (blue). In each case, the output trace shows a single pulse, either a fast pulse corresponding to the fundamental mode or a delayed pulse, which in this case corresponds to the HE_{21a} mode. The output beam shows clean and well defined profiles, corresponding to the respective simulated mode shapes. A micrograph of
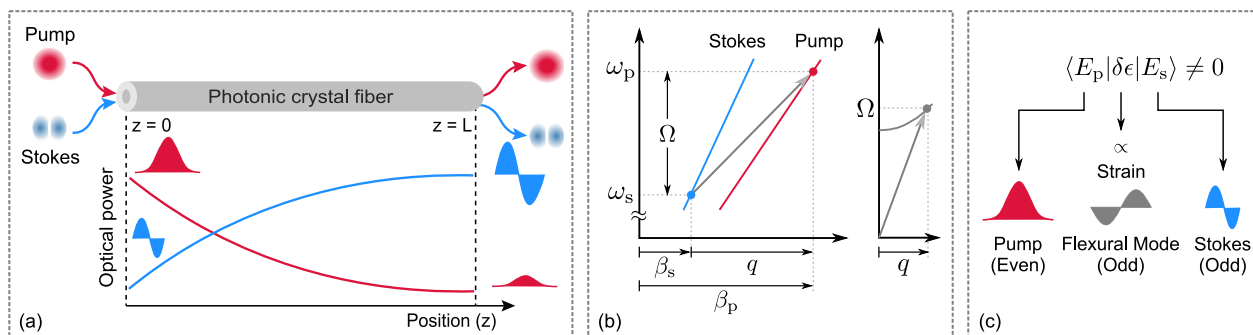
FIG. 1. (a) Schematic of energy transfer from the fundamental (pump) to a high-order anti-symmetric mode (Stokes) as they propagate along the fiber. (b) Optical (left) and mechanical (right) dispersion diagrams. Solid blue and red lines represent dispersion relations for pump and Stokes modes, respectively. The gray arrow corresponds to the inter-modal scattering. Phase-matching condition is also sketched at the bottom of the optical dispersion diagram. (c) Non-zero spatial overlap imposes a symmetry selection rule: symmetric fundamental mode and anti-symmetric high-order mode interact through an anti-symmetric mechanical flexural mode.
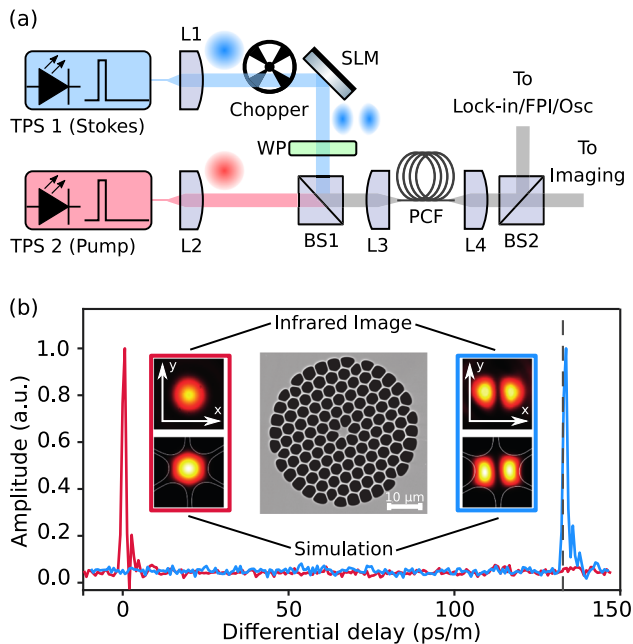
FIG. 2. (a) Experimental setup for inter-modal power conversion characterization in PCFs. TPS: tunable pulsed source; L: lens; SLM: spatial light modulator; WP: wave plate; BS: beam splitter; and FPI: scanning Fabry–Pérot interferometer. L3 and L4 are 50× microscope objective lenses. (b) Time series showing the differential delay corresponding to the HE_{11} and HE_{21a} modes. The dashed line corresponds to the position of the differential delay for the high-order mode, obtained by finite element method simulations. Experimental (top) and simulated (bottom) beam profiles for each scenario and SEM image of the PCF under study are shown in the insets.

the PCF used in our experiments is shown in Fig. 2(b), from which we measured the following parameters: $3.35 \pm 0.05 \ \mu$m solid-core diameter, $4.0 \pm 0.2 \ \mu$m cladding pitch, and $4.0 \pm 0.1 \ \mu$m cladding hole diameter. Both the differential delay and mode shape results compare well with simulations performed in Comsol Multiphysics [dashed lines and bottom inset images in Fig. 2(b)], employing the actual cross section extracted from the scanning electron microscope (SEM) image. Using the same short-pulse modulation, we also verified that the pump arm excites the fundamental mode with a high purity (no other modes are detected in time domain traces).

Once the mode excitation is optimized, we characterized the propagation and coupling losses for both HE_{11} and HE_{21a} modes using the cutback method. For a fiber length of 30 m, we obtained a propagation loss of 0.04 dB/m and coupling loss of 1.5 dB for HE_{11}, while for HE_{21a}, propagation and coupling losses were determined to be 0.15 dB/m and 4.5 dB, respectively. Although it is certainly possible to optimize the mode-launching scheme to minimize coupling losses in a practical device, it is not critical here for the purpose of demonstrating proof of principle.

To perform the FBS experiments, we switched to longer 80-ns square pulses at a repetition rate of 250 kHz, and each signal was individually amplified by erbium-doped fiber amplifiers, reaching peak powers of up to 2 W while preserving a relative low average power. The Stokes laser was kept at a constant operating wavelength, while the pump frequency was swept so that

different mechanical modes could be excited. The pump–Stokes frequency detuning was continuously monitored using an electrical spectrum analyzer. At the output of the fiber, the beam was split and one arm is monitored with an InGaAs camera, while the other is directed to two possible detection schemes, selected by a flip mirror. In the first scheme, we perform a broadband mechanical spectroscopy by sweeping the pump–Stokes frequency detuning over a wide range. Here, a novel detection scheme using a lock-in amplifier (LIA) is implemented to detect the mechanical resonance signatures. In the small gain-regime, the magnitude of the LIA signal is linearly proportional to the Brillouin gain spectrum (details regarding this approach can be found in Sec. S2.B of the supplementary material). While this technique is fast and does not require tunable narrow-band optical filters, it cannot discriminate between the Stokes gain or pump depletion since the chopper modulation is transferred from Stokes to pump due to the Brillouin interaction along the fiber. We therefore use a second detection scheme once a certain mechanical resonance is identified in the LIA spectrum. In this scheme, a scanning Fabry–Pérot interferometer (FPI) (7.5 MHz linewidth, 1.5 GHz free-spectral range) is employed to individually measure the pump and Stokes powers at the output of the fiber, and the energy transfer between the two signals can be quantitatively characterized.

IV. RESULTS

A. Intermodal FBS spectrum

Using the LIA detection method, we first obtained the inter-modal Brillouin spectrum shown in Fig. 3 for parallel and orthogonal pump-signal polarizations. Multiple mechanical resonances are observed, with two clearly dominant peaks centered at 1.30 GHz and 2.13 GHz and weaker resonances at 90 MHz and 750 MHz, and around 1.0 GHz and 1.75 GHz. No other significant resonances were observed between 2.5 GHz and 10.0 GHz. To better understand the features in the experimental spectrum and identify the mechanical modes responsible for each peak, we simulated the Brillouin gain for all modes supported by the PCF structure in the frequency range of interest. Details on the simulation can be found in Sec. S1 of the supplementary material. For the calculated Brillouin gain spectrum, the vertical axis represents Brillouin gain (normalized to the highest peak). Overall, the simulated spectrum semi-quantitatively explains the most important features observed in the experiment. Particularly, it is possible to identify the mechanical modes with highest gain and obtain the relative strengths of the strongest peaks. In addition, it gives insight on the observed polarization dependence. We now discuss these features in more detail.

In order to identify the mechanical modes related to the dominant peaks, we include simulated displacement profiles as insets in Fig. 3. These modes were calculated for a full PCF structure (obtained from the SEM profile) and compared to the corresponding modes in a suspended rod with the same core diameter. As expected, the flexural nature of these modes can be clearly observed, and moreover, the field profiles remarkably resemble those in a simple rod: all peaks correlate with flexural modes, A being the fundamental and B, C, and D being higher-order modes, with displacement nodes within the core region. Another important aspect is the twofold and threefold symmetry of these modes, which is critical to understand
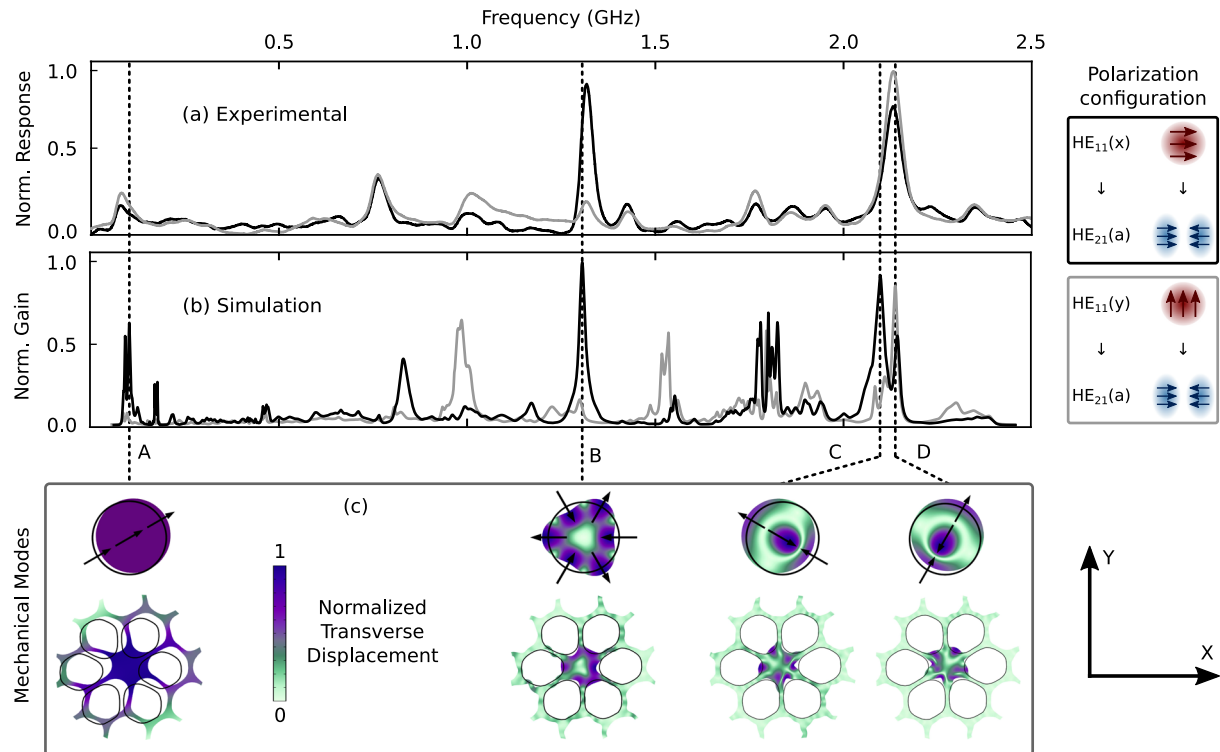
FIG. 3. (a) Experimental lock-in amplifier response (for 1 W of input power for each signal) and (b) simulated Brillouin gain spectra (normalized by the maximum peak), considering energy transfer between the HE_{11} and HE_{21a} modes for parallel (black) and crossed (gray) polarizations, as schematically suggested in the rightmost inset. The mechanical mode profiles for the selected A, B, C, and D peaks are shown in the bottom panel for both the realistic PCF model and a silica rod, with the same radius as the fiber core. The color scale represents the intensity of the transverse displacement in the cross section of the PCF.

the polarization dependence observed both in the experiments and simulations. Interestingly, the strongest mechanical resonances (peak B at 1.30 GHz and C/D at 2.13 GHz) present significantly different polarization dependency. On the one hand, at 2.13 GHz, we observe strong power exchange for both parallel and orthogonal polarization, while at 1.30 GHz only when pump and Stokes have orthogonal polarization. In other words, by selecting the frequency detuning, it is possible to create a device that is either dependent or virtually independent of the polarization.

The physical mechanism behind this observation is quite unique and not expected based on the simple rod analogy (where the peak at 1.3 GHz is polarization independent, contrary to our observation in a PCF). In a rod, there are two degenerate modes with a sixfold symmetry displacement profile at the 1.3 GHz region,[41] rotated by 30° relative to each other (one orientation is shown as mode B in Fig. 3). For parallel or orthogonal pump–probe polarization, only one or the other of these two orientations is excited, with, however, identical Brillouin gain (explaining why in a rod this peak is polarization independent). In a PCF, the picture changes. Even though both orientations of this mechanical mode are still present, one of them couples with the photonic crystal cladding much more strongly than the other. This hybridization with the cladding modes simply means that the mechanical energy for that particular orientation is no longer concentrated in the core, which leads to reducing its

overlap with the optical mode (thus lower Brillouin gain). The orientation that hybridizes with the cladding is exactly the one that would, in principle, couple orthogonal pump–probe polarizations, but, as observed experimentally and confirmed in the simulation, it does so very weakly. Physically, it is quite clear why one orientation couples to the cladding more strongly than the other. The sixfold symmetry of these two modes coincides with the sixfold symmetry of the photonic crystal cladding. This means that the mode whose maximum displacement lobes coincide with the glass webs hybridizes strongly, while the other, whose displacement nodes are aligned to the glass webs, does not.

We now turn to the mechanical modes giving rise to the polarization independent peak at 2.13 GHz. At about this same frequency, a rod supports two degenerate modes with a twofold symmetry, one rotated by 90° relative to the other. Again, one mode couples parallel polarization and the other orthogonal. Different than the previous sixfold mechanical modes, none of the twofold orientations hybridizes strongly with the cladding. Physically, the mismatch in symmetry (twofold vs sixfold) reduces the hybridization of the core modes with the photonic crystal cladding, and one can see in Fig. 3 that the mechanical energy is mostly concentrated in the core for both modes C and D. As a result, in the PCF, the orientation in C strongly couples parallel polarization, while the rotated mode in D couples orthogonal polarization, resembling the behavior in

a rod. This is also confirmed by numerical simulations (note, however, that these modes are no longer degenerate due to slight mechanical distortion in the structure).

It is worth pointing out that in some of the peaks, one can observe in both experiment and simulated spectra that their shapes deviate from a typical Lorentzian. This is because these peaks are formed from a cluster of several mechanical modes around their central frequency due to coupling between core and cladding vibrations. In addition, the pulsed excitation character convolved with the averaging in the LIA signal (which integrates the signal as the pump frequency is swept) effectively broadens the observed spectrum. Having said that, convolving the simulated spectrum with a filter equivalent to the experimental averaging (~ 15 MHz bandwidth) is not sufficient to fully explain the experiment (see, for example, a single peak at 2.13 GHz in the experiment while the simulation even after convolution shows two separate peaks). We point out that other possible reasons for this disagreement might be a mismatch between the actual and simulated fiber structure or fluctuations along the fiber length. Another aspect that upon careful observation might seem surprising is that the fundamental flexural mode at 90 MHz is not the dominant Brillouin peak. In a rod, one can show that the equivalent mode indeed exhibits the strongest Brillouin gain, and that is not the case in the PCF studied here, as observed experimentally and confirmed by the simulations. We will return to this point when we investigate in more detail the physical process dominating the strength of the optomechanical coupling as well as the damping mechanisms of the mechanical modes.

B. Intermodal FBS energy transfer

To quantitatively analyze the intermodal energy transfer at the most prominent Brillouin peaks, we performed a fine frequency scan and used the FPI detection scheme that allows discrimination between pump and Stokes signals. Initially, both have a fixed frequency separated by 2.13 GHz, corresponding to one of the Brillouin peaks in Fig. 3, and the FPI is scanned to measure the output power of each signal separately. The results are presented in Fig. 4(a) for three conditions: (i) both pump and Stokes on, (ii) only Stokes on, and (iii) only pump on. We used 1 W of input peak power for the Stokes and 2 W for the pump. Clearly, when both signals are present, a strong depletion of the pump is accompanied by a Stokes gain, as a result of the intermodal FBS process. A convenient way to quantify the energy transfer is the on/off gain, defined as the ratio of the Stokes output power levels with pump on and off. Analogously, the pump depletion is the ratio of the pump output power measured when the Stokes signal is turned on and off. The curves from Figs. 4(b) and 4(c) show the measured on/off Stokes gain and pump depletion for a narrow sweep around the 2.13 GHz frequency detuning. As the frequency separation approaches the Brillouin resonance, gain and depletion are maximized, reaching about 3 dB peak values. The solid lines represent numerical fitting that resulted in a Lorentzian curve with a 45 MHz FWHM. Performing a deconvolution of the signal with an effective Lorentzian accounting for the pulsed source and the FPI linewidth, we estimate a Brillouin linewidth of 42 MHz. We believe that the small asymmetry present in both curves can be attributed to the frequency-dependency of the single side-band modulator used to generate the Stokes signal
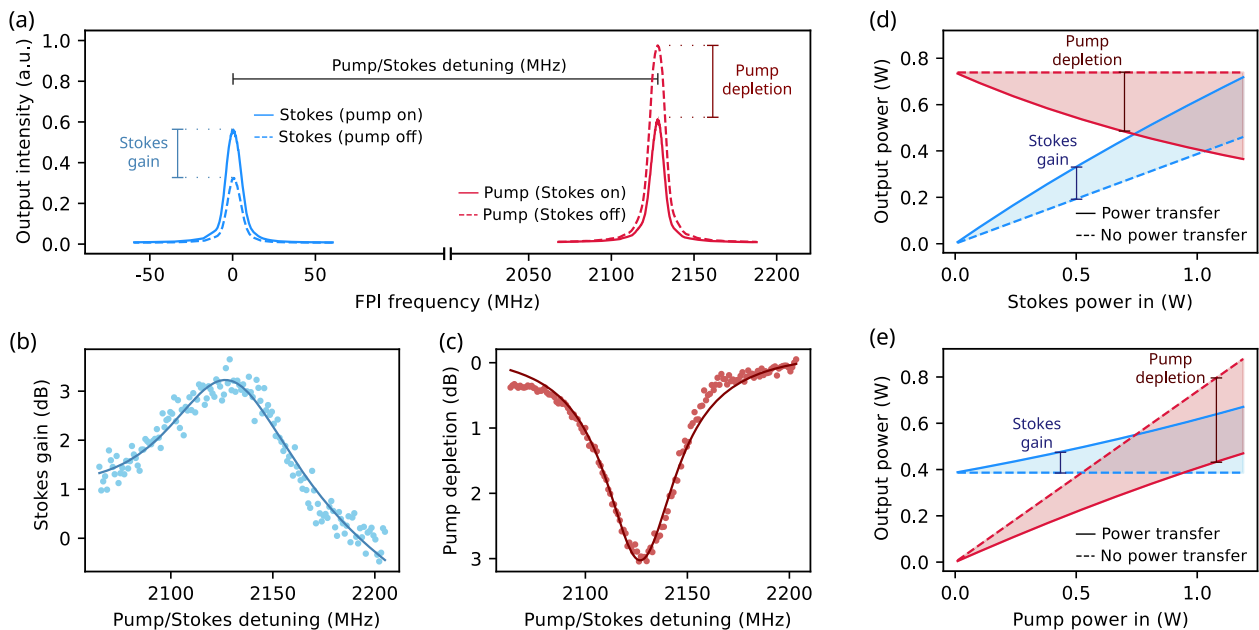
FIG. 4. (a) Examples of measured spectra using the FPI scheme. (b) and (c) Stokes on-off gain and pump on-off depletion vs detuning. (d) and (e) Measured Stokes (blue) and pump (red) output power levels as a function of Stokes and pump input power. For (d), pump input power was fixed at 1 W, while for (e), Stokes input power was fixed at 1 W. Dashed curves correspond to output power in the absence of Brillouin interaction (either pump or Stokes turned off), and solid curve correspond to both lasers interacting.

TABLE I. Gain coefficient values for the major observable Brillouin peaks for both polarization conditions.

Frequency (MHz)	Gain (parallel) ($W^{-1} km^{-1}$)	Gain (orthogonal) ($W^{-1} km^{-1}$)
90	6.1 ± 0.1	2.6 ± 0.1
1310	19.9 ± 0.2	3.9 ± 0.1
2130	19.2 ± 0.2	21.4 ± 0.3

for this measurement. For more information, see Sec. S2 of the supplementary material.

Figure 4(d) shows the evolution of the output power as the input Stokes power increases while keeping the pump input level constant. We can see that pump depletion increases with Stokes power, and at the levels experimentally available, we did not reach complete pump depletion. Similarly, Fig. 4(e) shows the output when the pump input power varies and Stokes is kept constant. Note that in both (d) and (e), the drop in pump power is not identical to the increase in Stokes power due to the different propagation losses of each mode.

To extract the gain coefficient, we can numerically solve the coupled equations in the FBS process and fit the experimental data (see Sec. S2.C of the supplementary material for details). We applied this procedure for three relevant Brillouin peaks by setting the corresponding pump–Stokes frequency detuning for parallel and orthogonal pump/Stokes polarization conditions. The results are summarized in Table I.

V. DISCUSSION AND CONCLUSIONS

From the experimental results listed in Table I, the highest gain coefficients are 21.4 $W^{-1} km^{-1}$ for a detuning of 2.13 GHz and 19.9 $W^{-1} km^{-1}$ for 1.31 GHz. In fact, this gain coefficient obtained in *forward* configuration in PCF is on the same order as observed in *backward* intermodal Brillouin scattering in FMFs.[24] This is quite remarkable because again, in all-solid fibers, forward Brillouin scattering involves mechanical modes that are distributed throughout the cladding with very little overlap with the optical modes. In PCF, transverse mechanical confinement enables high gain in forward configuration. Having said that, a more complete picture is provided here to better understand the physical limits and possible enhancement directions.

Fundamentally, the maximum Brillouin gain for a given resonance depends on the strength of the optomechanical coupling and on the linewidth of that particular resonance. It is therefore useful to separate the discussion of the optomechanical coupling strength from the damping mechanisms of the mechanical modes. In Fig. 5, for all mechanical modes, we plot separately g/Q, where g is the optomechanical gain coefficient and Q is the quality factor of the mechanical resonance. It is more convenient to look at Q^{-1} as we can directly add contributions from different damping mechanisms (i.e., $Q^{-1} = \sum_i Q_i^{-1}$). The number of mechanical modes in the complete structure is quite large and thus leads to very dense curves of the calculated coefficients. To help visualize the general trend, the results shown in this figure represent the envelop curves (highest g/Q and lowest $1/Q$), while the raw data for all modes can be found in the supplementary material.
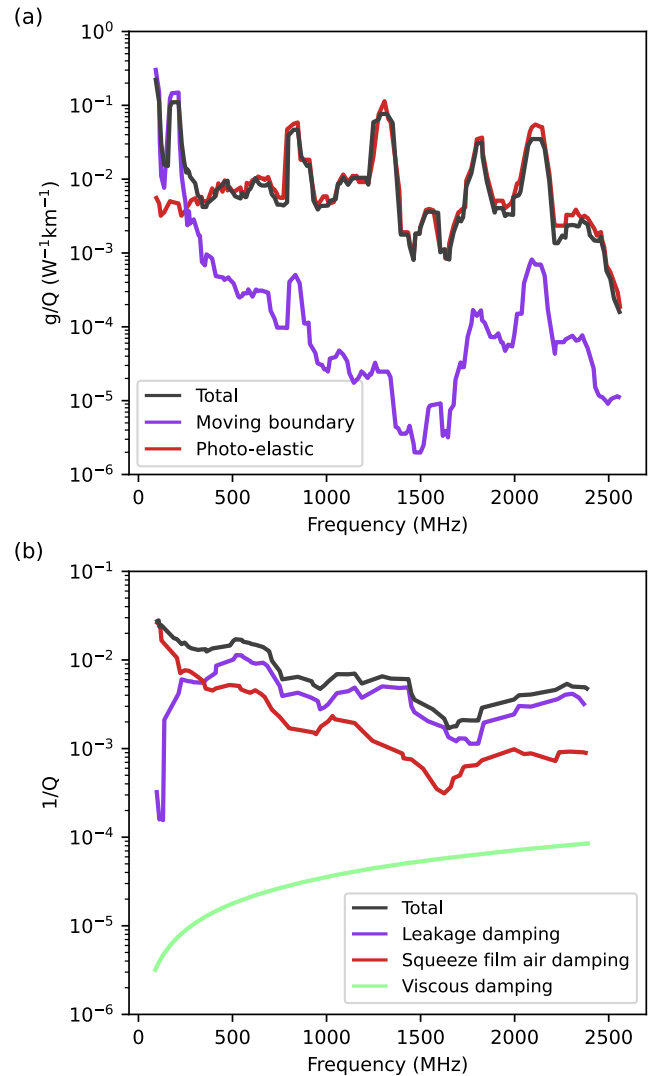
FIG. 5. (a) Calculated contributions to the net Brillouin gain (g/Q) from moving-boundary and photo-elastic effects. (b) Calculated contributions from different mechanisms to the total mechanical damping, represented as the inverse of the quality factor (Q^{-1}). Solid lines represent the envelope of the respective raw data, which is available in the supplementary material.

From the g/Q curves in Fig. 5(a), we can see that the lower frequency flexural modes indeed exhibit larger coupling strength (0.3 $W^{-1} km^{-1}$ for 90 MHz) than higher frequencies modes (0.04 $W^{-1} km^{-1}$ for 2.13 GHz), as expected from the suspended rod model. The results in Fig. 5(a) include contributions from moving-boundary and elasto-optic effects, which can reinforce or counter-act each other.[21,42] We can see that for the fundamental flexural modes, large optomechanical coupling is due to the moving-boundary contribution at the glass–air interface, a mechanism that is irrelevant in solid fibers given their small core-clad index contrast. For higher-order flexural modes, the elasto-optic mechanism dominates with overall lower g/Q values. Despite stronger

optomechanical coupling, our experiment shows that these low-frequency flexural modes do not dominate the Brillouin spectrum. This can be explained by evaluating the damping mechanisms shown in Fig. 5(b). Here, the lower frequency modes suffer the strongest damping (poorer quality factors), overriding their high optomechanical coupling. In this analysis, we considered three loss mechanisms for the mechanical modes: viscosity, leakage, and squeezed film air damping. Viscous damping scales quadratically with frequency ($\tau \propto 1/\omega_m^2$), which means that the quality factor would be inversely proportional to frequency if this was the dominant loss ($Q = \omega_m \tau \propto 1/\omega_m$), again favoring stronger Brillouin interaction at lower frequencies. However, it is clear from our modeling that viscosity is not the limiting factor, as shown in Fig. 5(b). Leakage through the cladding varies from mode to mode, and the profiles in Fig. 3 illustrate that some modes are more confined to the core than others. In the modeling, this was accounted for using a mechanical perfect matched layer at the outer silica cladding surface (see Sec. S1.B of the supplementary material for details). Leakage is dominant above 400 MHz, as shown in Fig. 5(b).

The main limitation for the low-frequency flexural modes arises from the effect of squeezed film air damping phenomenon, by which a micro-vibrating membrane transfers part of its energy to surrounding gas molecules.[43] Since there are many membranes vibrating in phase inside the PCF structure, this mechanism can be significant.[44] We used Bao's model[43] to estimate this contribution. From the results in Fig. 5(b), it is clear that squeezed film air damping is strongest for low order flexural modes, limiting their quality factors. For the 90 MHz peak, this mechanism lowers the quality factor from 1800 to 33, or in terms of linewidth broadening, it is increased from tens of kilohertz up to 3 MHz, consistent with the experimental value of ~5 MHz. At high frequencies, the calculated broadening due to squeezed film damping is negligible, and the obtained value of 35 MHz for the 2.13 GHz peak is consistent with the experimental value of 42 MHz. Another potential linewidth broadening factor not considered in the analysis here is the geometry non-uniformity along the fiber length. According to our simulations, a 5% geometry scaling results in 18% and 8% Brillouin frequency variation for 90 MHz and 2.13 GHz peaks, respectively. In other words, this form of inhomogeneous broadening due to geometry fluctuation might affect low frequency flexural modes more strongly than higher ones. When all damping effects are considered, the simulated gain values drop to 6.9 W^{-1} km^{-1}, 20.3 W^{-1} km^{-1}, and 19.6 W^{-1} km^{-1}, consistent with the experimental values from Table I. From a practical point of view, one could envision engineering structures that better confine mechanical modes to the core (i.e., reduce leakage) and rely on larger structure suspended-core fibers[45] to minimize squeezed film damping. In this ultimate scenario, the Brillouin gain for the 90 MHz flexural mode would be limited by viscosity as a fundamental mechanism and could potentially reach values higher than 1000 W^{-1} km^{-1}.

In conclusion, we demonstrated intermodal forward Brillouin scattering in PCF between the HE$_{11}$ and HE$_{21}$ modes over a wide range of frequencies (90 MHz–2.5 GHz), with a maximum gain coefficient of 21.4 W^{-1} km^{-1}. Symmetry arguments support the observation of polarization dependent and polarization-independent intermodal Brillouin interaction, and different damping mechanisms dictate the relative strength of FBS involving mechanical modes at low and high frequencies. This work opens the path to future engineering of PCF structures to enhance the interaction of optical modes of high order through the control of flexural mechanical modes and their dissipation mechanisms, leading ultimately to novel physical phenomena and highly efficient devices.

SUPPLEMENTARY MATERIAL

See the supplementary material for detailed explanations regarding the simulations, with in-depth information of each step and procedure (optical and mechanical modes, and Brillouin interactions), in addition to experimental considerations regarding the setup, excitation, and characterization of different modes, FBS frequency identification, and gain characterization.

AUTHORS' CONTRIBUTIONS

P.F.J. and E.L. contributed equally to this work.

DATA AVAILABILITY

The data that support the findings of this study are available from the corresponding author upon reasonable request.

REFERENCES

[1] D. J. Richardson, J. M. Fini, and L. E. Nelson, Nat. Photonics **7**, 354 (2013).
[2] G. Li, N. Bai, N. Zhao, and C. Xia, Adv. Opt. Photonics **6**, 413 (2014).
[3] A. Li, Y. Wang, Q. Hu, and W. Shieh, Opt. Express **23**, 1139 (2015).
[4] Y. Weng, E. Ip, Z. Pan, and T. Wang, Opt. Express **23**, 9024 (2015).
[5] M. Wang, H. Wu, M. Tang, Z. Zhao, Y. Dang, C. Zhao, R. Liao, W. Chen, S. Fu, C. Yang, W. Tong, P. P. Shum, and D. Liu, Opt. Express **25**, 4907 (2017).
[6] M. J. Murray, A. Davis, C. Kirkendall, and B. Redding, Opt. Express **27**, 28494 (2019).
[7] L.-C. Hsu, T.-C. Chen, Y.-T. Yang, C.-Y. Huang, D.-W. Shen, Y.-T. Chen, and M.-C. M. Lee, Lab Chip **13**, 1151 (2013).
[8] J. Parker, C. W. Peterson, Y. Yifat, S. A. Rice, Z. Yan, S. K. Gray, and N. F. Scherer, Optica **7**, 1341 (2020).
[9] Z. Yan, R. A. Shah, G. Chado, S. K. Gray, M. Pelton, and N. F. Scherer, ACS Nano **7**, 1790 (2013).
[10] X. Ji, J. K. Jang, U. D. Dave, M. Corato-Zanarella, C. Joshi, A. L. Gaeta, and M. Lipson, Laser Photonics Rev. **15**, 2000353 (2020).
[11] E. A. Kittlaus, N. T. Otterstrom, P. Kharel, S. Gertler, and P. T. Rakich, Nat. Photonics **12**, 613 (2018).
[12] N. T. Otterstrom, E. A. Kittlaus, S. Gertler, R. O. Behunin, A. L. Lentine, and P. T. Rakich, Optica **6**, 1117 (2019).
[13] C. Koebele, M. Salsi, D. Sperti, P. Tran, P. Brindel, H. Mardoyan, S. Bigo, A. Boutin, F. Verluise, P. Sillard, M. Astruc, L. Provost, F. Cerou, and G. Charlet, Opt. Express **19**, 16593 (2011).

[14] G. Labroille, B. Denolle, P. Jian, P. Genevaux, N. Treps, and J.-F. Morizur, Opt. Express **22**, 15599 (2014).

[15] A. Forbes, A. Dudley, and M. McLaren, Adv. Opt. Photonics **8**, 200 (2016).

[16] N. K. Fontaine, R. Ryf, H. Chen, D. T. Neilson, K. Kim, and J. Carpenter, Nat. Commun. **10**, 1865 (2019).

[17] S. G. Leon-Saval, N. K. Fontaine, J. R. Salazar-Gil, B. Ercan, R. Ryf, and J. Bland-Hawthorn, Opt. Express **22**, 1036 (2014).

[18] A. M. Velázquez-Benítez, J. E. Antonio-López, J. C. Alvarado-Zacarías, N. K. Fontaine, R. Ryf, H. Chen, J. Hernández-Cordero, P. Sillard, C. Okonkwo, S. G. Leon-Saval *et al.*, Sci. Rep. **8**, 8897 (2018).

[19] K. Solehmainen, M. Kapulainen, M. Harjanne, and T. Aalto, IEEE Photonics Technol. Lett. **18**, 2287 (2006).

[20] N. Andermahr and C. Fallnich, Opt. Express **18**, 4411 (2010).

[21] G. S. Wiederhecker, P. Dainese, and T. P. Mayer Alegre, APL Photonics **4**, 071101 (2019).

[22] P. S. J. Russell, D. Culverhouse, and F. Farahi, IEEE J. Quantum Electron. **27**, 836 (1991).

[23] K. Y. Song, Y. H. Kim, and B. Y. Kim, Opt. Lett. **38**, 1805 (2013).

[24] K. Y. Song and Y. H. Kim, Opt. Lett. **38**, 4841 (2013).

[25] A. Li, Q. Hu, and W. Shieh, Opt. Express **21**, 31894 (2013).

[26] X. Huang and S. Fan, J. Lightwave Technol. **29**, 2267 (2011).

[27] M. S. Kang, A. Butsch, and P. S. J. Russell, Nat. Photonics **5**, 549 (2011).

[28] Y. Liu, A. Choudhary, G. Ren, D.-Y. Choi, A. Casas-Bedoya, B. Morrison, P. Ma, T. G. Nguyen, K. Vu, A. Mitchell, S. J. Madden, D. Marpaung, and B. J. Eggleton, in *Conference on Lasers and Electro-Optics* (Optical Society of America, 2019), p. STh1J.4.

[29] E. A. Kittlaus, N. T. Otterstrom, and P. T. Rakich, Nat. Commun. **8**, 15819 (2017).

[30] J. R. Koehler, R. E. Noskov, A. A. Sukhorukov, A. Butsch, D. Novoa, and P. S. J. Russell, APL Photonics **1**, 056101 (2016).

[31] P. S. J. Russell, D. Culverhouse, and F. Farahi, Electron. Lett. **26**, 1195 (1990).

[32] N. Shibata, A. Nakazono, N. Taguchi, and S. Tanaka, IEEE Photonics Technol. Lett. **18**, 412 (2006).

[33] P. Dainese, P. S. J. Russell, N. Joly, J. C. Knight, G. S. Wiederhecker, H. L. Fragnito, V. Laude, and A. Khelif, Nat. Phys. **2**, 388 (2006).

[34] P. Dainese, P. S. J. Russell, G. S. Wiederhecker, N. Joly, H. L. Fragnito, V. Laude, and A. Khelif, Opt. Express **14**, 4141 (2006).

[35] D. Elser, U. L. Andersen, A. Korn, O. Glöckl, S. Lorenz, C. Marquardt, and G. Leuchs, Phys. Rev. Lett. **97**, 133901 (2006).

[36] J.-C. Beugnot, T. Sylvestre, H. Maillotte, G. Mélin, and V. Laude, Opt. Lett. **32**, 17 (2007).

[37] J.-C. Beugnot, T. Sylvestre, D. Alasia, H. Maillotte, V. Laude, A. Monteville, L. Provino, N. Traynor, S. F. Mafang, and L. Thévenaz, Opt. Express **15**, 15517 (2007).

[38] A. Brenn, G. S. Wiederhecker, M. S. Kang, H. Hundertmark, N. Joly, and P. S. J. Russell, J. Opt. Soc. Am. B **26**, 1641 (2009).

[39] M. S. Kang, A. Brenn, and P. S. J. Russell, Phys. Rev. Lett. **105**, 153901 (2010).

[40] C. Wolff, R. V. Laer, M. J. Steel, B. J. Eggleton, and C. G. Poulton, New J. Phys. **18**, 025006 (2016).

[41] C. Wolff, M. J. Steel, and C. G. Poulton, Opt. Express **22**, 32489 (2014).

[42] O. Florez, P. F. Jarschel, Y. A. Espinel, C. Cordeiro, T. M. Alegre, G. S. Wiederhecker, and P. Dainese, Nat. Commun. **7**, 11759 (2016).

[43] M. Bao and H. Yang, Sens. Actuators, A **136**, 3 (2007).

[44] J. R. Koehler, A. Butsch, T. G. Euser, R. E. Noskov, and P. S. J. Russell, Appl. Phys. Lett. **103**, 221107 (2013).

[45] L. Dong, B. K. Thomas, and L. Fu, Opt. Express **16**, 16423 (2008).